

# Numerical Heat Transfer, Part A: Applications

## An International Journal of Computation and Methodology

ISSN: (Print) (Online) Journal homepage: <https://www.tandfonline.com/loi/unht20>

# Soret–Dufour mass transfer effects on radiative chemically dissipative MHD plain convective water nanofluid ( $\text{Al}_2\text{O}_3$ , Cu, Ag, & $\text{TiO}_2$ ) flow across a temperature-controlled upright cone surface with heat blow/suction

Elumalai Ragulkumar, Paulsamy Sambath, Krishnan Suresh, Sivasamy Balasubramanian & Ali J. Chamkha

To cite this article: Elumalai Ragulkumar, Paulsamy Sambath, Krishnan Suresh, Sivasamy Balasubramanian & Ali J. Chamkha (09 Oct 2023): Soret–Dufour mass transfer effects on radiative chemically dissipative MHD plain convective water nanofluid ( $\text{Al}_2\text{O}_3$ , Cu, Ag, &  $\text{TiO}_2$ ) flow across a temperature-controlled upright cone surface with heat blow/suction, Numerical Heat Transfer, Part A: Applications, DOI: [10.1080/10407782.2023.2261624](https://doi.org/10.1080/10407782.2023.2261624)

To link to this article: <https://doi.org/10.1080/10407782.2023.2261624>



Published online: 09 Oct 2023.



Submit your article to this journal [↗](#)



View related articles [↗](#)



View Crossmark data [↗](#)



# Soret–Dufour mass transfer effects on radiative chemically dissipative MHD plain convective water nanofluid ( $\text{Al}_2\text{O}_3$ , Cu, Ag, & $\text{TiO}_2$ ) flow across a temperature-controlled upright cone surface with heat blow/suction

Elumalai Ragulkumar<sup>a</sup> , Paulsamy Sambath<sup>a</sup> , Krishnan Suresh<sup>b</sup>, Sivasamy Balasubramanian<sup>c</sup>, and Ali J. Chamkha<sup>d</sup>

<sup>a</sup>Department of Mathematics, SRM Institute of Science and Technology, Kattankulathur, Chennai, Tamil Nadu, India; <sup>b</sup>Department of Chemical Engineering, SRM Institute of Science and Technology, Kattankulathur, Chennai, Tamil Nadu, India; <sup>c</sup>Department of Chemical Engineering, KPR Institute of Engineering and Technology, Coimbatore, Tamil Nadu, India; <sup>d</sup>Faculty of Engineering, Kuwait College of Science and Technology, Doha District, Kuwait

## ABSTRACT

In the current analysis, we delivered a computational approach to the 2D boundary layer heat and mass transfer flow of water-based nanofluids over a vertical cone saturated by porous media with heat generation/absorption, thermal radiation, chemical reactions, the Soret–Dufour number, viscous dissipation, and a magnetic field. The controlling partial differential equations are converted into devoid of dimensions form and numerically dealt with by Crank–Nicolson through an implicit finite difference approach. Specifically, the given parameters, such as volume fraction ( $\phi$ ), MHD–Magnetohydrodynamics (M), Soret/Dufour (Sr–Du), viscous dissipation ( $\epsilon$ ), chemical reaction ( $\lambda$ ), thermal radiation (Rd), and heat blowing/suction ( $\Delta$ ), have an impact on boundary layer flow characteristics (velocity, temperature, concentration, drag coefficient, rate of heat transfer, and mass transfer rate) are thoroughly studied, and the outcomes are visually and tabulated to demonstrate the actual significance of the problem.

## ARTICLE HISTORY

Received 3 April 2023  
Revised 28 June 2023  
Accepted 2 August 2023

## KEYWORDS

Chemical reaction; dissipation; finite difference; free convection; mass transfer; MHD; nanofluids; radiation; Soret–Dufour effect; vertical cone

## 1. Overview

Natural convection is a prevalent occurrence in which convective flow is naturally established in a liquid body as a consequence of the formation of a pressure differential caused by a gradient of temperature. Natural convection occurs when a fluid close to a hot source absorbs heat, and as a result of thermal expansion, it becomes less dense and rises. In its location, a lighter or warmer liquid displaces the adjacent colder liquid. A current of convection is created as a result of heating this colder fluid once more and continuing the process. It has numerous uses, including temperature management, biological systems, and thermal energy preservation. The chilling of electrical and electronic parts, air conditioner elements, and equipment in the steel industry all benefit greatly from natural convection. Plain convective is favored for cooling since it does not require any moving parts, making it quieter and more compact. Choi and Eastman [1] delivered the first report of such work in this technique, combining various metals and metal oxides to generate a nanosubstance. The procedure described by Xuan and Li [2] involves mixing



The effect of thermal radiation on an incompressible viscous fluid passing through a vertically inclined plate in an unstable laminar free convective MHD flow under the influence of a heat source and sink is studied by Sambath *et al.* [13]. Sambath *et al.* [14] studied the characteristics of a heat source, chemically reacting radiative, viscous dissipative MHD flow of an incompressible viscous fluid through an upright cone under inhomogeneous mass flux. The influence of cross-diffusion on the drag coefficient, the thermal as well as mass transference from an upright cone in a spongy media was studied by Awad *et al.* [15]. An illustration of 2D MHD heat and mass transfer boundary layer flow through saturated porous media by Sreedevi *et al.* [16] is presented. Rashad and Chamkha [17] investigated the impact of  $Du$  and  $Sr$  on heat and species transfer in a non-darcy convective boundary layer flow around a permeable frustum cone. Reddy and Chamkha [18] used  $Sr/Du$  effects, thermal radiation, and a magnetic field to investigate the flow of heat and mass transfer properties of water-based nanofluids over a stretched sheet via a porous media. Mohiddin *et al.* [19] analyzed the flow of heat and mass flux in an incompressible laminar boundary layer around a vertical stationary cone driven by viscoelastic buoyancy. Mohiddin and Varma [20] explored the numerical analysis of buoyancy-driven, unsteady natural convection boundary layer flow across a vertical cone embedded in a non-Darcian isotropic porous regime. This mathematical model's heat and mass flux technique is based on water nanofluid flows *via* an upright cone and has been examined by Ragulkumar *et al.* [21] for MHD, radiation, and chemical reactions.

The MHD of a water-based nanofluid flow *via* an upright cone is examined in this paper by Ragulkumar *et al.* [22] using a mathematical approach. The heat and mass transfer properties of an inclined vertical plate embedded in a porous medium were studied by Reddy *et al.* [23]. Chamkha [24, 25] used distinct geometry to associate thermal as well as species transmission by plain convective in the effect of an MHD and  $Rd$  effect. The flow of an electrically conducting and heat-generating/absorbing fluid in a channel embedded in a homogeneous porous media is described by Chamkha and Quadri Ali [26] as a non-Darcian mixed convection flow. A permeable horizontal cylinder immersed in a homogeneous porous medium was used in Prabhavathi *et al.* [27] study that investigated coupled heat and mass transport by natural convection in the presence of the magnetic field, porous medium inertia, and heat generation/absorption effects.

It is a study dealing with the Soret/Dufour phenomena on plain convective nanofluid flow across a vertical porous cone surface with various quantities of thermal as well as mass transference. It is investigated how thermal and mass are transferred from the cone to the nanofluid by immersing it in a fluid containing nanoparticles. The part that examines whether the occurrence of thermal and species transfer alters with the inclusion of fluid parameters. Furthermore, we have visually demonstrated how thermal and mass current conditions affect nanofluid attributes during heat and species transmission.

On the upright conical application side, the conical continuous mixers have their main purpose of constantly mixing, loading, and releasing the mix until all tasks are completed, or a work break occurs. The ingredients are constantly loaded into this mixer by screw feeders. Conical continuous mixers are frequently the ideal choice for high-volume tasks that require quickness and effectiveness. Additionally, our more flexible mixer, the conical continuous mixer, can be utilized to mix a variety of goods, including cookies, batters, icings, and pastes. The majority of cookies and any other application where components must be blended prior to adding flour work best with a conical continuous mixer.

In the event conical continuous mixers are used, the effectiveness of the grinding process is noticeable as the mixer warms up on the cone's slope surface. The temperature is conducted over the surface of the cone as a result of the mixture being rapidly and frequently mixed. The elevated temperature of the heated cone was then convective to its environs; this article goes into depth about the heat transmission in these processes as well as their parametric properties.

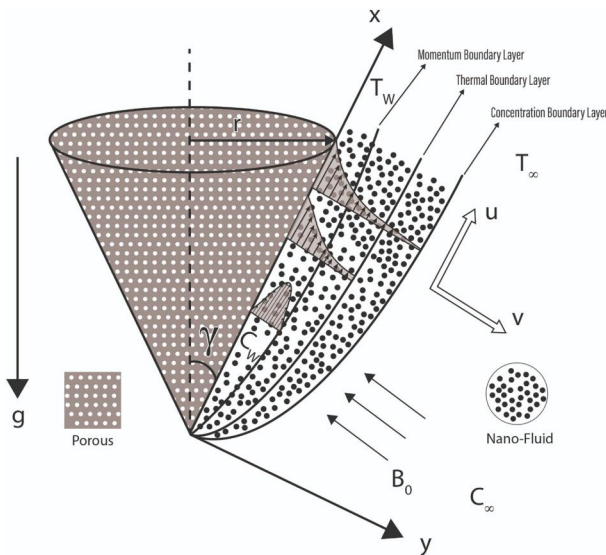


Figure 1. Physical model.

## 2. Analysis of flow problem

In this study, the magnetohydrodynamic (MHD) radiative nanofluid flow over an up-straight cone porous surface has been investigated. This work has taken into account the impact of viscous dissipation, chemical reaction, thermal radiation, and Soret/Dufour effects to manage heat and mass transfer. The flow develops in an upward direction as a consequence of the cone's radius and half-angle being specified by  $r$  and  $\gamma$ , respectively. The first and second terms on the right side of velocity equation (Eq. (2)) are the thermal and species buoyancy terms, and the hydromagnetic drag term is the last. The second component on the right side of temperature equation (Eq. (3)) is associated with thermal radiation, the third term is the heat source/sink term, the fourth term is the Dufour effect, and the last term is the viscous dissipation term. The second and final component in the diffusion equation (Eq. (4)) is referred to as the Soret effect and corresponds to a first-order chemical process.

A vertical cone of half-angle  $\gamma$  embedded in a porous medium with Soret and Dufour effects results in boundary layer flow because of natural convection. As portrayed in Figure 1, the vertex of the entire cone serves as the origin of the coordinate system, with  $x$  expressing the coordinate along the cone's surface measured from the origin and  $y$  denoting the coordinate perpendicular to the conical surface. The ambient thermal reading (temperature) and species are always lower than  $T_w$  and  $C_w$ , respectively, that is,  $T_w > T_\infty$  and  $C_w > C_\infty$ . The ambient temperature as well as concentration are denoted by the notations  $T_\infty$  and  $C_\infty$ . A buoyancy force term is based on the assumption that fluid properties are constant except for density variations. The controlling equations for flow, thermal, and species transmission inside the periphery layer near the upright cone can be represented in 2D coordinates ( $x, y$ ), supposing that the thermal and species periphery layers are appropriately thin relative to the nearby radius.

The basis of dimensional governing equations and the Boussinesq approximation are given as Equation of Continuity

$$\frac{\partial(ru)}{\partial x} + \frac{\partial(rv)}{\partial y} = 0 \quad (1)$$

## Equation of Momentum

$$\frac{\partial u}{\partial t'} + u \frac{\partial u}{\partial x} + v \frac{\partial u}{\partial y} = g \frac{(\rho\beta_T)_{nf}}{\rho_{nf}} (T' - T'_\infty) \cos\gamma + g \frac{(\rho\beta_C)_{nf}}{\rho_{nf}} (C' - C'_\infty) \cos\gamma + \nu_{nf} \frac{\partial^2 u}{\partial y^2} - \frac{\nu_{nf} u}{k_0} - \frac{\sigma B_0^2}{\rho_{nf}} u \quad (2)$$

## Equation of Energy

$$\frac{\partial T'}{\partial t'} + u \frac{\partial T'}{\partial x} + v \frac{\partial T'}{\partial y} = \frac{1}{(\rho c_p)_{nf}} \left[ k_{nf} \frac{\partial^2 T'}{\partial y^2} + \mu_{nf} \left( \frac{\partial u}{\partial y} \right)^2 - \frac{\partial q_r}{\partial y} + Q_0 (T' - T'_\infty) + \frac{D_m K_T}{C_s C_p} \left( \frac{\partial^2 C}{\partial y^2} \right) \right] \quad (3)$$

## Equation of Concentration

$$\frac{\partial C'}{\partial t'} + u \frac{\partial C'}{\partial x} + v \frac{\partial C'}{\partial y} = D \frac{\partial^2 C'}{\partial y^2} - K_1 (C' - C'_\infty) + \frac{D_m K_T}{T_m} \left( \frac{\partial^2 T}{\partial y^2} \right) \quad (4)$$

Initial as well as periphery conditions are

$$\begin{aligned} t' \leq 0 : u = 0, v = 0, T' = T'_\infty, C' = C'_\infty \quad \text{for all } x \text{ and } y \\ t' > 0 : u = 0, v = 0, T'(x) = T'_\infty + ax^n, C'(x) = C'_\infty + ax^m \quad \text{at } y = 0 \\ u = 0, T' = T'_\infty, C' = C'_\infty \quad \text{at } x = 0 \\ u = 0, T' \rightarrow T'_\infty, C' \rightarrow C'_\infty \quad \text{as } y \rightarrow \infty \end{aligned} \quad (5)$$

where  $q_w(x) = ax^n, q_w^*(x) = bx^n$ .

The density  $\rho_{nf}$ , thermal expansion coefficient  $(\rho\beta)_{nf}$ , and heat capacitance  $(\rho c_p)_{nf}$  expressions for nanofluids are presented.

$$\begin{aligned} \rho_{nf} &= (1 - \phi)\rho_f + \phi\rho_s \\ (\rho\beta)_{nf} &= (1 - \phi)(\rho\beta)_f + \phi(\rho\beta)_s \\ (\rho c_p)_{nf} &= (1 - \phi)(\rho c_p)_f + \phi(\rho c_p)_s \\ \frac{k_{nf}}{k_f} &= \frac{k_s + (n - 1)k_f - (n - 1)\phi(k_f - k_s)}{k_s + (n - 1)k_f + \phi(k_f - k_s)} \\ \frac{\mu_{nf}}{\mu_f} &= \frac{1}{(1 - \phi)^{2.5}} \end{aligned}$$

The following nondimensional variables are introduced [14, 21]:

$$\begin{aligned} X = \frac{x}{L}, Y = \frac{y}{L}, Gr_L^{1/4}, U = \frac{uL}{\nu_f} Gr_L^{-1/2}, V = \frac{vL}{\nu_f} Gr_L^{-1/4}, t = \frac{\nu_f t' (Gr_L)^{1/2}}{L^2} \\ T = \frac{T' - T'_\infty}{T'_W - T'_\infty}, C = \frac{C' - C'_\infty}{C'_W - C'_\infty}, Gr_L = \frac{g\beta_f (T'_W - T'_\infty) L^3 \cos\gamma}{\nu_f^2}, \\ Gr_C = \frac{g\beta_f (C'_W - C'_\infty) L^3 \cos\gamma}{\nu_f^2}, Pr = \frac{\nu_f}{\alpha_f}, \lambda = \frac{K_1 L^2}{\nu_f} Gr_L^{-1/2}, \frac{1}{K} = \frac{L^2}{k_0} \\ M = \frac{\sigma B_0^2 L^2}{\mu_f} Gr_L^{-1/2}, Sc = \frac{\nu_f}{D}, \Delta = \frac{Q_0 L^2}{\nu_f (\rho c_p)_f} Gr_L^{-1/2}, Sr = \frac{D_m K_T (T'_W - T'_\infty)}{T_m \nu_f (C'_W - C'_\infty)} \\ Du = \frac{D_m K_T}{C_s C_p \nu_f} \frac{C'_W - C'_\infty}{T'_W - T'_\infty}, Rd = \frac{k_1^* k}{4\sigma^* T_\infty^3}, N = \frac{Gr_C}{Gr_L}, \epsilon = \frac{g\beta L}{(c_p)_f}, R = \frac{r}{L}; \quad r = x \sin \gamma. \end{aligned}$$

The radiative heat flow  $q_r$  is calculated using the Roseland approximation [24] and is represented by

$$q_r = -\frac{4\sigma^*}{3K^*} \frac{\partial T'^4}{\partial y} \quad (6)$$

Given that the temperature variations within the flow are sufficiently modest,  $T'^4$  may be written as a temperature-dependent linear function. Then, in the Taylor series about  $T'_\infty$ , extending  $T'^4$  while ignoring higher-order terms has the form

$$T'^4 \cong 4T'_\infty T' - 3T'^2_\infty \quad (7)$$

Substituting Eqs. (6) and (7) in Eq. (3), we have

$$\frac{\partial T'}{\partial t'} + u \frac{\partial T'}{\partial x} + v \frac{\partial T'}{\partial y} = \frac{1}{(\rho c_p)_{nf}} \left[ k_{nf} \frac{\partial^2 T'}{\partial y^2} + \mu_{nf} \left( \frac{\partial u}{\partial y} \right)^2 + Q_0(T' - T'_\infty) - \frac{16\sigma^* T'_\infty}{3K^*} \frac{\partial^2 T'}{\partial y^2} + \frac{D_m K_T}{C_s C_p} \left( \frac{\partial^2 C}{\partial y^2} \right) \right] \quad (8)$$

Equation of Continuity

$$\frac{\partial U}{\partial X} + \frac{\partial V}{\partial Y} + \frac{U}{X} = 0 \quad (9)$$

Equation of Momentum

$$\frac{\partial U}{\partial t} + U \frac{\partial U}{\partial X} + V \frac{\partial U}{\partial Y} = A_1 \left[ A_2(T) + A_3(NC - MU) - \frac{1}{(1-\phi)^{2.5}} \left( KU - \frac{\partial^2 U}{\partial Y^2} \right) \right] \quad (10)$$

Equation of Energy

$$\frac{\partial T}{\partial t} + U \frac{\partial T}{\partial X} + V \frac{\partial T}{\partial Y} = A_4 \left[ \frac{k_{nf}}{k_f} \frac{1}{Pr} \frac{\partial^2 T}{\partial Y^2} - \frac{1}{Pr} \left( \frac{3R_d + 4}{3R_d} \right) + \Delta T + Du \frac{\partial^2 C}{\partial Y^2} + \frac{1}{(1-\phi)^{2.5}} \epsilon \left( \frac{\partial U}{\partial Y} \right)^2 \right] \quad (11)$$

Equation of Concentration

$$\frac{\partial C}{\partial t} + U \frac{\partial C}{\partial X} + V \frac{\partial C}{\partial Y} = \frac{1}{Sc} \frac{\partial^2 C}{\partial Y^2} + Sr \frac{\partial^2 T}{\partial Y^2} - \lambda C \quad (12)$$

where,  $A_1 = \frac{1}{(1-\phi) + \phi \left( \frac{\rho \beta}{\rho_f} \right)}$ ,  $A_2 = ((1-\phi) + \phi \left( \frac{\rho \beta}{\rho_f} \right))$ ,  $A_3 = (1-\phi) + \phi \left( \frac{\rho \beta}{\rho_f} \right)$ ,  $A_4 = \frac{1}{(1-\phi) + \phi \left( \frac{\rho c_p}{\rho c_{pf}} \right)}$ , Form of dimensionless initial and periphery conditions are

$$\begin{aligned} t' \leq 0 : & \quad U = 0, V = 0, T = 0, C = 0 & \text{for all } X \text{ and } Y \\ t' > 0 : & \quad U = 0, V = 0, T = 1, C = 1 & \text{at } Y = 0 \\ & \quad U = 0, T = 0, C = 0 & \text{at } X = 0 \\ & \quad U \rightarrow 0, T \rightarrow 0, C \rightarrow 0 & \text{as } Y \rightarrow \infty \end{aligned} \quad (13)$$

The form of dimensionless local coefficient of drag, the local rate of heat, and mass transmissions are the relevant physical quantities and are each described as

$$\begin{aligned} \tau_X &= \frac{1}{(1-\phi)^{2.5}} Gr^{3/4} \left( \frac{\partial U}{\partial Y} \right)_{Y=0} \\ Nu_X &= \frac{k_{nf}}{k_f} \frac{-X \left( \frac{\partial T}{\partial Y} \right)_{Y=0} Gr^{1/4}}{T_{Y=0}} \\ Sh_X &= \frac{-X \left( \frac{\partial C}{\partial Y} \right)_{Y=0} Gr^{1/4}}{C_{Y=0}} \end{aligned}$$

Additionally, the dimensionless average coefficient of drag, average rate of heat, and mass transmission are described as follows:

$$\begin{aligned}\bar{\tau} &= \frac{2}{(1-\phi)^{2.5}} Gr^{3/4} \int_0^1 X \left( \frac{\partial U}{\partial Y} \right)_{Y=0} dX \\ \bar{N}_u &= 2 \frac{k_{nf}}{k_f} Gr^{1/4} \int_0^1 \frac{-X \left( \frac{\partial T}{\partial Y} \right)_{Y=0}}{T_{Y=0}} dX \\ \bar{S}h &= 2Gr^{1/4} \int_0^1 \frac{-X \left( \frac{\partial C}{\partial Y} \right)_{Y=0}}{C_{Y=0}} dX\end{aligned}$$

### 3. Finite difference formulation

All the guiding PDEs (9)–(12) incorporating initial and periphery conditions (13) are solved using implicit finite difference schemes of the Crank–Nicolson type used throughout this work. Using the relevant finite difference operator with grid discretization, the aforementioned PDEs (9–12) are first transformed into finite difference equations that can be numerically computed, as shown below:

$$\begin{aligned}\frac{U_{i,j}^{k+1} - U_{i-1,j}^{k+1} + U_{i,j}^k - U_{i-1,j}^k + U_{i,j}^{k+1} - U_{i-1,j-1}^{k+1} + U_{i,j}^k - U_{i-1,j-1}^k}{4\Delta X} \\ + \frac{V_{i,j}^{k+1} - U_{i,j-1}^{k+1} + U_{i,j}^k - U_{i,j-1}^k}{2\Delta Y} + \frac{U_{i,j}^{k+1} - U_{i,j-1}^{k+1} + U_{i,j}^k - U_{i,j-1}^k}{4i\Delta X} = 0\end{aligned}\quad (14)$$

$$\begin{aligned}\frac{U_{i,j}^{k+1} - U_{i,j}^k}{\Delta t} + U_{i,j}^k \frac{U_{i,j}^{k+1} - U_{i-1,j}^{k+1} + U_{i,j}^k - U_{i-1,j}^k}{2\Delta X} + V_{i,j}^k \frac{U_{i,j+1}^{k+1} - U_{i,j-1}^{k+1} + U_{i,j+1}^k - U_{i,j-1}^k}{4\Delta Y} \\ = A_1 \left[ \frac{A_2}{2} (T_{i,j}^{k+1} + T_{i,j}^k) + \frac{A_3}{2} (N(C_{i,j}^{k+1} + C_{i,j}^k) - M(U_{i,j}^{k+1} + U_{i,j}^k)) \right] \\ + A_4 \frac{U_{i,j-1}^{k+1} - 2U_{i,j}^{k+1} + U_{i,j+1}^{k+1} + U_{i,j-1}^k - 2U_{i,j}^k + U_{i,j+1}^k}{2(\Delta Y)^2}\end{aligned}\quad (15)$$

$$\begin{aligned}\frac{T_{i,j}^{k+1} - T_{i,j}^k}{\Delta t} + U_{i,j}^k \frac{T_{i,j}^{k+1} - T_{i-1,j}^{k+1} + T_{i,j}^k - T_{i-1,j}^k}{2\Delta X} + V_{i,j}^k \frac{T_{i,j+1}^{k+1} - T_{i,j-1}^{k+1} + T_{i,j+1}^k - T_{i,j-1}^k}{4\Delta Y} \\ = A_5 \left[ \frac{k_{nf}}{k_f} \frac{1}{Pr} \left( \frac{T_{i,j-1}^{k+1} - 2T_{i,j}^{k+1} + T_{i,j+1}^{k+1} + T_{i,j-1}^k - 2T_{i,j}^k + T_{i,j+1}^k}{2(\Delta Y)^2} \right) - \frac{1}{Pr} \left( \frac{3R_d + 4}{3R_d} \right) \right. \\ \left. (T_{i,j}^{k+1} + T_{i,j}^k) + \frac{\Delta}{2} (T_{i,j}^{k+1} + T_{i,j}^k) + Du \left( \frac{C_{i,j-1}^{k+1} - 2C_{i,j}^{k+1} + C_{i,j+1}^{k+1} + C_{i,j-1}^k - 2C_{i,j}^k + C_{i,j+1}^k}{2(\Delta Y)^2} \right) \right] \\ + A_6 \epsilon \left( \frac{U_{i,j+1}^{k+1} - U_{i,j-1}^{k+1} + U_{i,j+1}^k - U_{i,j-1}^k}{4\Delta Y} \right)^2\end{aligned}\quad (16)$$

$$\begin{aligned}\frac{C_{i,j}^{k+1} - C_{i,j}^k}{\Delta t} + U_{i,j}^k \frac{C_{i,j}^{k+1} - C_{i-1,j}^{k+1} + C_{i,j}^k - C_{i-1,j}^k}{2\Delta X} + V_{i,j}^k \frac{C_{i,j+1}^{k+1} - C_{i,j-1}^{k+1} + C_{i,j+1}^k - C_{i,j-1}^k}{4\Delta Y} \\ = \frac{1}{Sc} \frac{C_{i,j-1}^{k+1} - 2C_{i,j}^{k+1} + C_{i,j+1}^{k+1} + C_{i,j-1}^k - 2C_{i,j}^k + C_{i,j+1}^k}{2(\Delta Y)^2} \\ + Sr \left( \frac{T_{i,j-1}^{k+1} - 2T_{i,j}^{k+1} + T_{i,j+1}^{k+1} + T_{i,j-1}^k - 2T_{i,j}^k + T_{i,j+1}^k}{2(\Delta Y)^2} \right) - \frac{\lambda}{2} (C_{i,j}^{k+1} + C_{i,j}^k)\end{aligned}\quad (17)$$

The  $x$  and  $y$  axes' respective mesh positions are shown by  $(i, j)$ . Evidently, the terms  $\Delta X, \Delta Y$ , and  $\Delta t$  refer to the phase dimensions in  $X, Y$ , and  $t$ , respectively, while the terms  $(n, n + 1)$

indicate  $n^{\text{th}}$  and  $(n + 1)^{\text{th}}$  loops expressing for U, T, with C. The FDEs of velocity, thermal reading (temperature), and species can be calculated using well-chosen invariant values. The derived finite difference algorithm equations must be translated into an algebraic system of equations. These algebraic tri-diagonal equations can possibly be solved using the Thomas technique. The phase dimensions in the  $\Delta X$  and  $\Delta Y$  axes have the value 0.05, the time step is set to  $\Delta t = 0.01$ , and the boundary conditions that correspond to  $y \rightarrow \infty$  are denoted by  $X_{\text{max}} = 1$  and  $Y_{\text{max}} = 20$ , respectively. The state of being in steady state happens when the variable being tested achieves the tolerance level of  $10^{-5}$ . Since the truncate problem in the FDM is  $O(\Delta t^2 + \Delta Y^2 + \Delta X)$  and approaches zero as  $\Delta t, \Delta Y$ , and  $\Delta X \rightarrow 0$ , it is obvious that the system is compatible. Also, the Crank–Nicolson system is always stable. The combination of compatibility and stability ensures convergence. The Newton–Cotes closed integration formula is used to evaluate integrals. A five-point approximation is used to assess the derivatives of dimensionless equations involving local and average drag coefficients, local and average thermal transmit coefficients (Nusselt numbers), and local and average species transference coefficients.

#### 4. Result and discussion

Our aim is to highlight the role of physics in the system of flow by analyzing the effects of radiative variable (Rd), magnetic parameter (M), viscous dissipation ( $\epsilon$ ), chemical reaction ( $\lambda$ ), Soret (Sr), Dufour (Du) effects, heat blowing/sink ( $\Delta$ ), volume fraction ( $\phi$ ), and nanoparticle types ( $\text{Al}_2\text{O}_3$ , Cu, Ag, and  $\text{TiO}_2$ ) on spatial velocity, temperature, and concentration within the boundary layer in Figures 2–7. Here,  $\text{Pr} = 6.2$ ,  $\text{Sc} = 0.61$ ,  $M = 0.5$ ,  $\lambda = 0.5$ ,  $\Delta = 0.5$ ,  $K = 1$ ,  $\epsilon = 0.5$ ,  $\text{Rd} = 1$ ,  $\text{Sr} = 0.30$ , and  $\text{Du} = 0.20$  are the default parameter values used in all finite difference computations.

To represent the diffusion-thermo and thermal-diffusion effects, respectively, Dufour (Du) and Soret (Sr) are nondimensional parameters that, by definition, can take on any value, provided that the value of their respective products remains constant. As a result, it is anticipated that, in the current scenario, the outcome will constantly remain the same (0.06), provided that the reference temperature  $T_\infty$  and mean temperature  $T_m$  are both kept constant. Figures 8–10 depict a plot of the impacts of the drag coefficient, heat transfer rate, and mass transfer rate in the presence of a cone-shaped porous surface, with a number of informative parameters ( $\Delta$ , Rd, M,  $\lambda$ ,  $\epsilon$ , Sr, and Du) being used.

In Tables 2–4, the local skin friction, local Nusselt number, and Sherwood number values for the nanofluids made of  $\text{Al}_2\text{O}_3$  and Cu are compared. A rising (M) value indicates an increase in the local friction coefficient because of magnetic interactions among atoms contributing to sliding friction, while a decreasing local Nusselt number and Sherwood number indicates a slower rate of nanoparticle dissolution into water is evident in both  $\text{Al}_2\text{O}_3$  and Cu nanofluids. It is shown that a rise in the local Nusselt number and Sherwood number corresponds to more active convection in both Cu and  $\text{Al}_2\text{O}_3$  nanofluids, but a reserve pattern is seen in the skin friction coefficient with growing values of ( $\phi$ ). Furthermore, these tables show that the skin-friction coefficient and the local Nusselt number decline, whereas local skin friction increases as (Rd) grows for both  $\text{Al}_2\text{O}_3$  and Cu nanofluids. According to reports, the local skin friction declines in Cu while it rises in  $\text{Al}_2\text{O}_3$  with greater ( $\lambda$ ) values. As the quantity ( $\lambda$ ) grows, the local Nusselt number in the Cu enhances and reduces  $\text{Al}_2\text{O}_3$ . Sherwood number increases in both nanofluids with ( $\lambda$ ).

##### 4.1. Nanofluids

A representative velocity, temperature, and concentration profile for various nanofluids is presented in Figure 2, where  $M = 1$ ,  $K = 1$ ,  $\text{Rd} = 0.4$ ,  $\text{Sr} = 0.20$ ,  $\text{Du} = 0.30$ ,  $\lambda = 1$ ,  $\Delta = 1$ , and  $\epsilon = 0.6$  are different dimensionless coordinates. As compared to other nanoparticles, silver causes

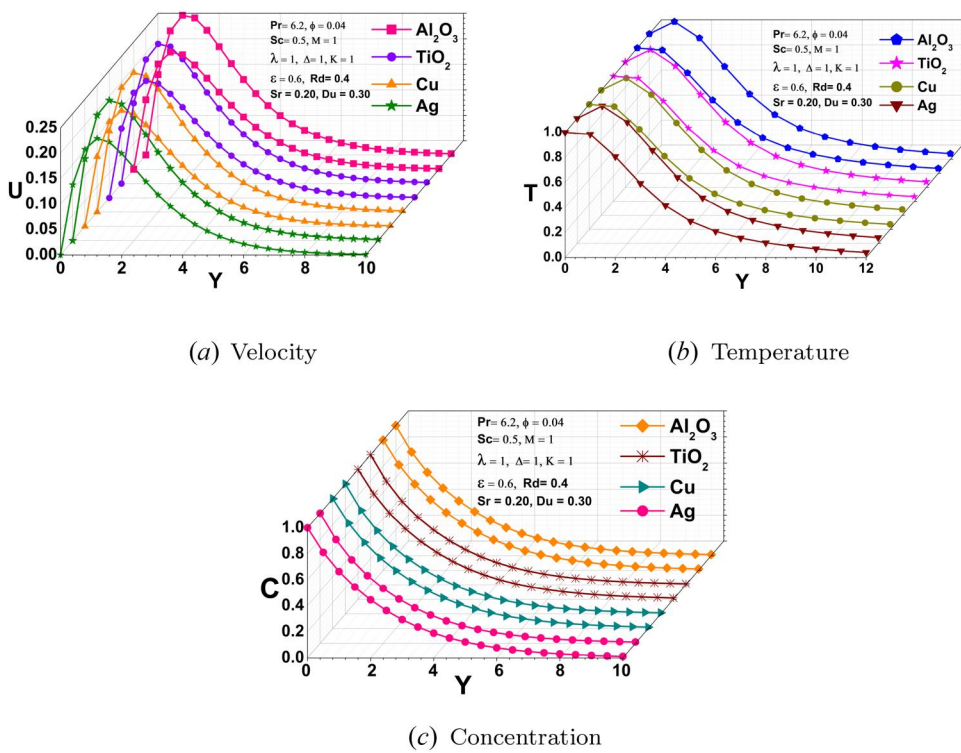


Figure 2. Different nanofluid.

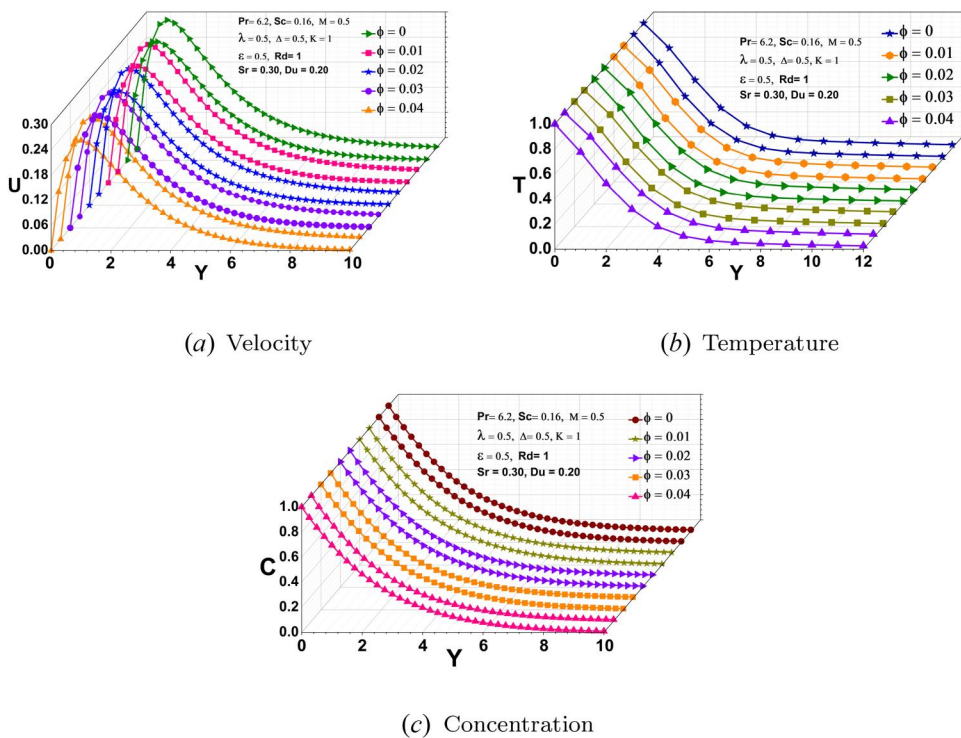


Figure 3. Different  $\phi$ .

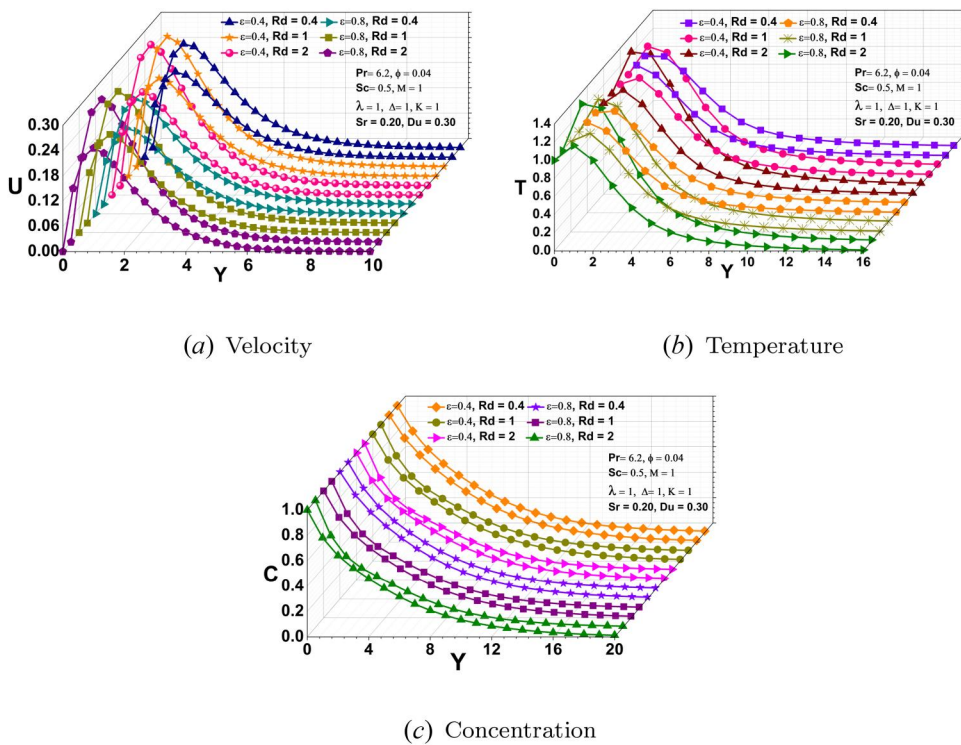


Figure 4. Various  $\epsilon$  and  $Rd$ .

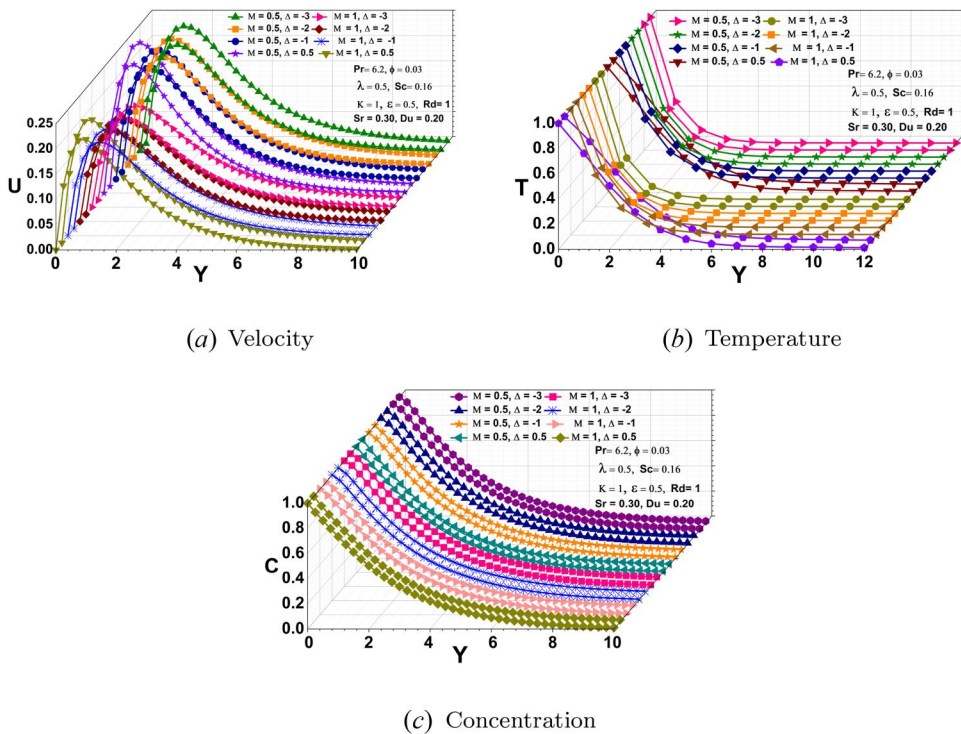
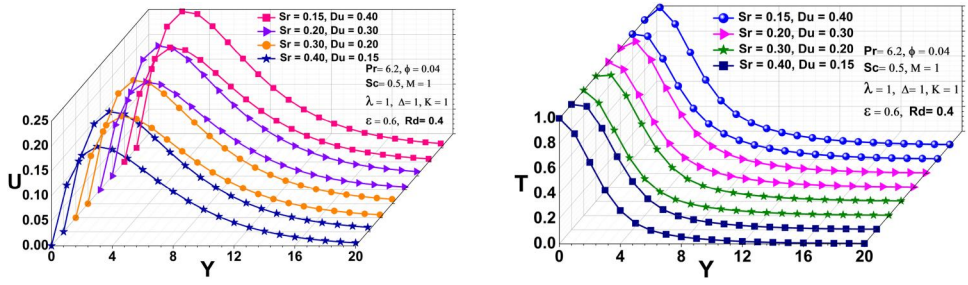
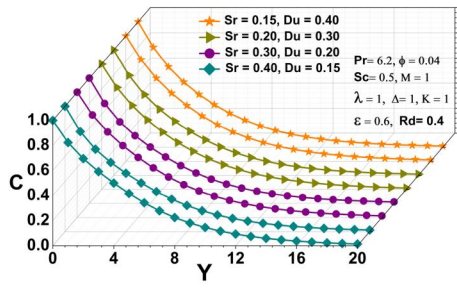


Figure 5. Various  $M$  and  $\Delta$ .



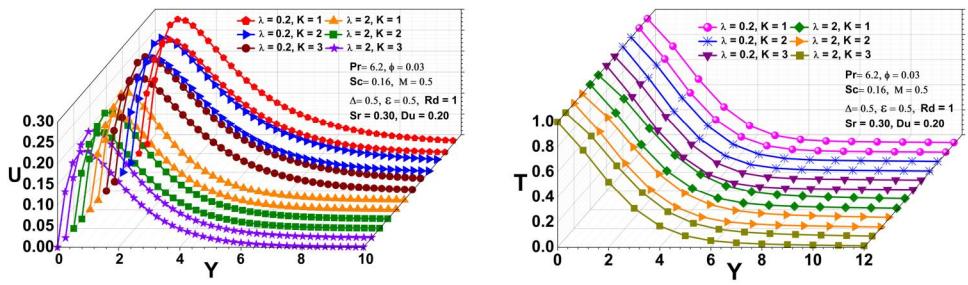
(a) Velocity

(b) Temperature



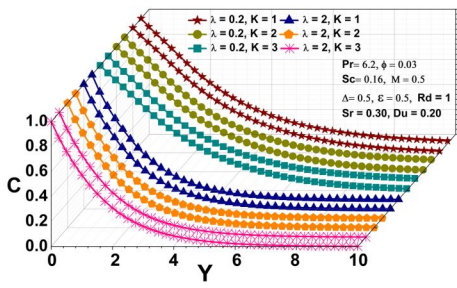
(c) Concentration

Figure 6. Various Sr and Du.



(a) Velocity

(b) Temperature



(c) Concentration

Figure 7. Different  $\lambda$  and K.

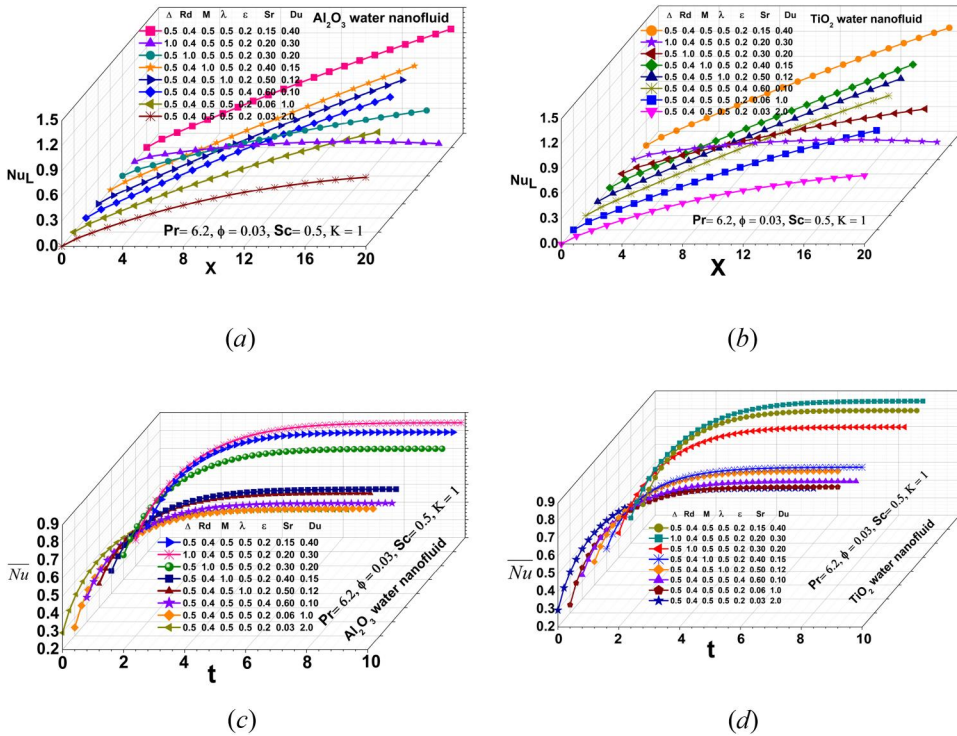


Figure 8. Local and average Nusselt number for varying parameters.

high heat and mass transfer because of its viscous nature. In the graph, neither the temperature nor concentration profiles show any noticeable change. However, based on the numerical values, copper has a higher heat transfer capacity at velocity and temperature because delocalized electrons inside metal lattices have the flexibility to travel freely within their lattice. In comparison, silver has a higher heat transfer capacity at concentration, which has to do with its valence and crystal structure.

#### 4.2. Volume fractions

A typical profile of velocity, temperature, and concentration along a cone is shown in Figure 3 for different values of  $\phi$  in the presence of a porous surface. The volume fraction increases as the velocity and temperature rise because of the working fluid's conductive heat transfer coefficient climbing. The increase in the working fluid's conductive heat transfer coefficient enhances the conductive transmission of thermal energy within the working fluid, but the  $C$  (concentration) is only declining. Moreover, the fluid resistance would rise as viscosity increased. This shows that as the volume fraction grows, substantially higher forces are necessary to induce the liquid to flow. Additionally, the  $\phi$  represents the volume fraction of nanoparticles ( $\text{Al}_2\text{O}_3$ , Cu, Ag, and  $\text{TiO}_2$ ) in the nanofluid, as shown in Table 1. It characterizes the concentration of nanoparticles within the base fluid (water). The presence and concentration of nanoparticles influence the thermophysical properties of the nanofluid and can affect the overall heat transfer and fluid flow behavior.

#### 4.3. Viscous dissipation and radiation

The velocity, temperature, and concentration profiles are influenced by the  $\epsilon$  and  $Rd$ , as illustrated in Figure 4. As  $\epsilon$  and  $Rd$  increase, the heat transfer from a cone rises, affecting velocity

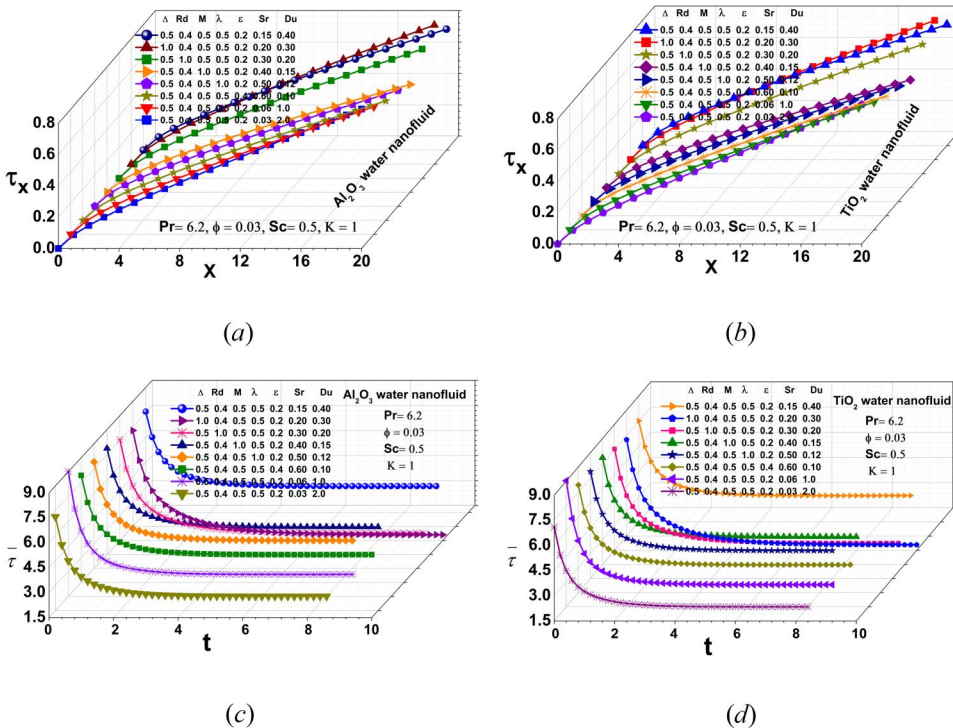


Figure 9. Local and average skin friction for varying factors.

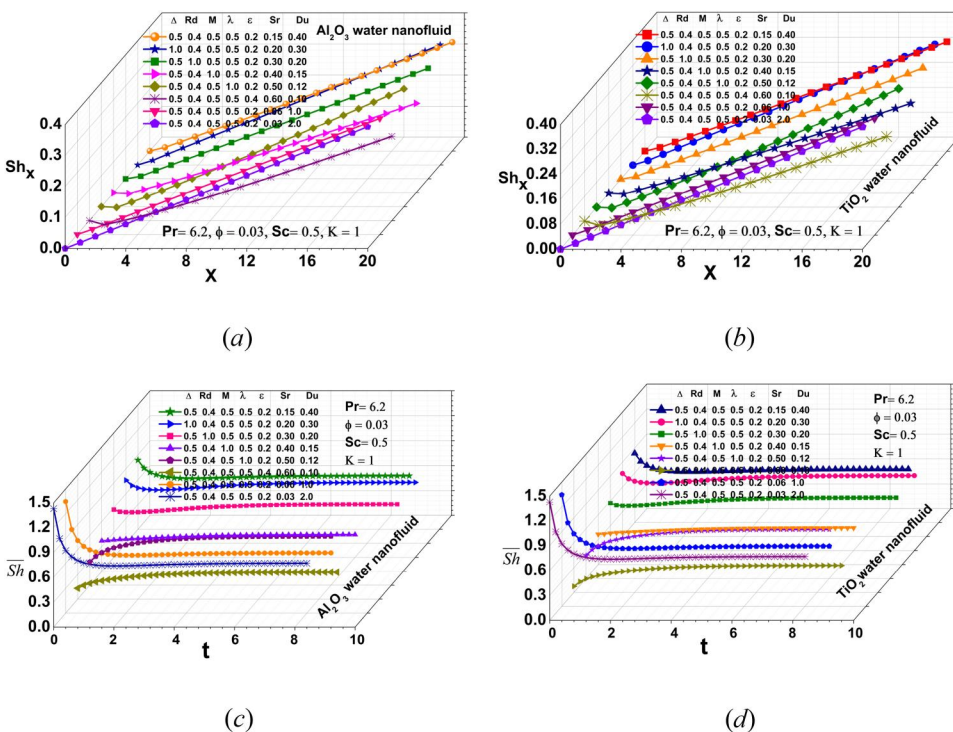


Figure 10. Local and average Sherwood number for various parameters.

**Table 1.** Water and nanoparticles: thermophysical characteristics [22].

Physical attributes	Water	Aluminum oxide	Copper	Titanium dioxide	Silver
$\bar{\rho}$ ( $kg/m^3$ )	997.10	3970.0	8933.0	4250.0	10500
$\beta \times 10^{-5}$ ( $K^{-1}$ )	21.0	0.85	1.67	0.90	1.89
$k$ ( $W/mk$ )	0.613	40.0	401.0	8.9538	429
$C_p$ ( $J/kgK$ )	4179.0	765.0	385.0	686.2	235

**Table 2.** Skin-friction coefficient as a function of several factors ( $\tau_x$ ).

Local skin friction				Prabhavathi et al. [24]		Present results	
Parameters				$Al_2O_3$	Cu	$Al_2O_3$	Cu
M	$\phi$	Rd	$\lambda$				
0.1	0.01	0.1	0.1	1.01431	0.97482	1.01562	0.97731
0.5	0.01	0.1	0.1	1.11614	1.07839	1.11217	1.08002
0.7	0.01	0.1	0.1	1.21037	1.17657	1.21123	1.17912
1.0	0.01	0.1	0.1	1.29734	1.26555	1.29854	1.26732
0.5	0.01	0.1	0.1	1.14833	0.94507	1.14872	1.94717
0.5	0.02	0.1	0.1	0.99597	0.97550	0.99012	0.97823
0.5	0.03	0.1	0.1	0.84003	0.83044	0.84113	0.83131
0.5	0.04	0.1	0.1	0.74516	0.74349	0.74721	0.74719
0.5	0.01	0.1	0.1	1.14833	1.11692	1.14911	1.11714
0.5	0.01	0.3	0.1	1.13967	1.10531	1.14001	1.10813
0.5	0.01	0.5	0.1	1.13254	1.10000	1.13516	1.10031
0.5	0.01	0.7	0.1	1.12655	1.05700	1.12913	1.05913
0.5	0.01	0.1	0.1	1.04128	0.98206	1.04316	0.98413
0.5	0.01	0.1	0.4	1.02721	0.96602	1.02801	0.96812
0.5	0.01	0.1	0.7	1.01772	0.95718	1.01823	0.95802
0.5	0.01	0.1	1.0	1.01055	0.95038	1.01111	0.95071

**Table 3.** Influence of several variables on the local Nusselt number  $Nu_L$ .

Local Nusselt number				Prabhavathi et al. [24]		Present results	
Parameters				$Al_2O_3$	Cu	$Al_2O_3$	Cu
M	$\phi$	Rd	$\lambda$				
0.1	0.01	0.1	0.1	0.49084	0.31626	0.49132	0.31708
0.5	0.01	0.1	0.1	0.47354	0.30166	0.47521	0.30231
0.7	0.01	0.1	0.1	0.45705	0.28654	0.45913	0.28732
1.0	0.01	0.1	0.1	0.43626	0.26152	0.43821	0.26261
0.5	0.01	0.1	0.1	0.46802	0.30868	0.46914	0.30911
0.5	0.02	0.1	0.1	0.51035	0.31226	0.51211	0.31308
0.5	0.03	0.1	0.1	0.56129	0.33590	0.56231	0.33641
0.5	0.04	0.1	0.1	0.59870	0.36021	0.60102	0.36091
0.5	0.01	0.1	0.1	0.46802	0.29651	0.46915	0.29688
0.5	0.01	0.3	0.1	0.42031	0.26681	0.42210	0.26710
0.5	0.01	0.5	0.1	0.38330	0.24387	0.38432	0.24401
0.5	0.01	0.7	0.1	0.35362	0.22567	0.35511	0.22604
0.5	0.01	0.1	0.1	0.49125	0.32426	0.49209	0.32509
0.5	0.01	0.1	0.4	0.49597	0.32692	0.49714	0.32699
0.5	0.01	0.1	0.7	0.49872	0.32853	0.49905	0.32871
0.5	0.01	0.1	1.0	0.50059	0.32964	0.50102	0.33002

and temperature profiles as a result of the irreversible effort made by the motion of fluid to overcome the layers of shear forces in the flow, which appears as a rise in fluid temperature and velocity. This is primarily the result of viscous dissipation, which affects fluid temperature, reducing fluid density, and thermal radiation, which is the result of accelerated charged particles emitting electromagnetic radiation. Specifically, as  $\epsilon$  and Rd increase, the concentration decreases as the difference in temperature between the wall and the fluid increases in the medium region. Viscous dissipation refers to the conversion of mechanical energy into thermal energy because of fluid

**Table 4.** Local Sherwood number depending on various parameters ( $Sh_x$ ).

Local Sherwood number				Prabhavathi et al. [24]		Present results	
Parameters				$Al_2O_3$	$TiO_2$	$Al_2O_3$	$TiO_2$
M	$\phi$	Rd	$\lambda$				
0.1	0.01	0.1	0.1	0.67366	0.68898	0.67408	0.68910
0.5	0.01	0.1	0.1	0.65936	0.67407	0.65947	0.67422
0.7	0.01	0.1	0.1	0.64667	0.66065	0.64681	0.66072
1.0	0.01	0.1	0.1	0.63594	0.64987	0.63614	0.64996
0.5	0.01	0.1	0.1	0.65496	0.68645	0.65511	0.68651
0.5	0.02	0.1	0.1	0.67280	0.68168	0.67304	0.68184
0.5	0.03	0.1	0.1	0.69595	0.69961	0.69608	0.69980
0.5	0.04	0.1	0.1	0.71197	0.71266	0.71205	0.71272
0.5	0.01	0.1	0.1	0.65496	0.66895	0.65507	0.66902
0.5	0.01	0.3	0.1	0.65857	0.67226	0.65879	0.67231
0.5	0.01	0.5	0.1	0.66158	0.67451	0.66179	0.67462
0.5	0.01	0.7	0.1	0.66412	0.67633	0.66419	0.67641
0.5	0.01	0.1	0.1	0.67549	0.69705	0.67568	0.69720
0.5	0.01	0.1	0.4	0.87924	0.89158	0.87971	0.89172
0.5	0.01	0.1	0.7	1.04113	1.04960	1.04113	1.04975
0.5	0.01	0.1	1.0	1.17977	1.18618	1.17998	1.18629

friction. The  $\epsilon$  quantifies the importance of this dissipation process. It affects the temperature distribution and can influence fluid flow patterns. Herewith, Rd represents the radiative effects within the flow. It accounts for the transfer of thermal energy through radiation; Rd influences the temperature distribution within the boundary layer.

#### 4.4. MHD and heat sink/source

A change in M and  $\Delta$  influences velocity, temperature, and concentration profiles in Figure 5. In the boundary layer region, our observations show a decrease in temperature and velocity distributions of porous surfaces as M and  $\Delta$  increase due to the Lorentz force that a magnetic field produces, which opposes motion and consequently slows it down. A rise in concentration can also be observed with increasing M and  $\Delta$ . This representation in Figure 5 is primarily due to the heat source/sink parameter and its thermal conductivity, which consequently raises and reduces the fluid temperature. In the same way, MHD offers control over separation flows, fluid manipulation, and optimized heat transfer from electrically conducting fluids. M is a measure of the influence of magnetic field strength on the fluid flow. It characterizes the MHD effects. The presence of a magnetic field can alter the fluid motion and heat transfer characteristics in the system. Heat blowing/suction refers to the localized heat transfer from or to the surface.  $\Delta$  represents the intensity of this heat transfer. It can be used to control the boundary conditions and affect the temperature distribution near the surface.

#### 4.5. Soret and Dufour

Figure 6 shows the changes in heat and mass transfer that result from increasing Soret's effect while decreasing Dufour's influence when these two processes take place simultaneously at the porous surface. The fluctuation of Sr and Du had a considerable influence on velocity and temperature; as a result, velocity and temperature decreased because higher Soret numbers were associated with a lower temperature gradient, which causes less convective movement, as well as a smaller mass concentration gradient that happens as a result of related irreversible mechanisms. It is an inverse phenomenon of the Soret effect. Thus, under the impact of Sr and Du, the concentration rises. The Soret effect refers to the mass transport induced by a temperature gradient. Sr characterizes the influence of the thermal gradient on the mass transfer within the fluid flow.

It affects the concentration distribution in the boundary layer. The Dufour effect represents the heat transport induced by a concentration gradient.  $Du$  quantifies the influence of the concentration inclination on the heat transfer within the fluid flow. It affects the temperature distribution in the boundary layer.

#### 4.6. Chemical reaction and porous media

As illustrated in Figure 10, the swings in velocity, temperature, and concentration profiles are connected to various chemical reaction parameters ( $\lambda$ ) and porous values ( $K$ ). In the presence of increasing chemical reaction parameters ( $\lambda$ ) and porosity ( $K$ ), velocity and temperature profiles decrease significantly. As the value of ( $\lambda$ ) rises, the velocity and temperature also rise due to the molecules colliding more often with each other as they move around; there is a higher probability that the reaction will occur. As a result, a faster reaction rate is achieved; however, as ( $K$ ) rises, the velocity and temperature stay almost constant until gradually declining as the value decreases. Concentration drops when ( $\lambda$ ) increases, but as ( $K$ ) increases, there is no significant change, and in some regions, it tends to increase. As the concentration of reactants lowers, the reactants have a more difficult time finding each other to react with; hence, the rate of reaction slows down. As a result, as time progresses as well as concentrations of reactants decline, the rate of reaction reduces.  $\lambda$  represents the presence of chemical reactions within the fluid flow. It accounts for the conversion or transformation of species because of chemical reactions. The presence of chemical reactions can significantly impact the temperature and concentration profiles.

#### 4.7. Nusselt number

Figure 8a–8d depicts the influence of numerous factors on the local as well as the average rate of heat transmission of  $Al_2O_3$  and  $TiO_3$  nanofluids. Significant benefits are gained when nanoparticles are correctly diffused in the base fluid, including better heat conduction, decreased erosion risk, higher thermal conductivity, and mixture stability. Changing the parameters in this example has an impact on the local and average heat transfer rate, but the atomic chain behavior makes it such that the given values have the opposite impact. The local Nusselt number declines somewhat unexpectedly because the exact heat transfer coefficient at that particular region of interest initially lowers as the amount of the heat source increases, but the average Nusselt number increases since it represents the average value over the whole surface. The results reveal that altering the length of the heat source has a greater impact on the flow and thermal fields than changing the position of the heat source. When the aspect ratio of the obstruction and the length of the heat source rises, the average Nusselt number correspondingly rises.

#### 4.8. Skin friction

In Figure 9a–9d, we show the variation in the local as well as average coefficients of drag for  $Al_2O_3$  as well as  $TiO_2$  nanofluids as a function of quantities ( $Rd$ ,  $\lambda$ ,  $\Delta$ ,  $\epsilon$ ,  $M$ ,  $Sr$ , and  $Du$ ). Additionally, local skin friction increases with parameter increase, except for the chemical process, which is assumed to be true for  $Al_2O_3$  and  $TiO_2$ , while average friction rises for all other factors except  $Rd$  and  $Du$ . Skin friction, which happens when a fluid scrapes against the surface of a moving object, is solely responsible for this. It increases and enlarges with the square of the velocity in proportion to the surface area in contact with the fluid. The nature and level of roughness of the surfaces in contact define the coefficient of static friction force. This undoubtedly contributes to surface area or size. The coefficient of skin friction against an external surface increases significantly in the low-pressure regime as load increases, while it becomes mostly insensitive to pressure after reaching a critical pressure value.

#### 4.9. Sherwood number

Figure 10a–10d illustrates the impact of varying ( $Rd$ ,  $\lambda$ ,  $\Delta$ ,  $\epsilon$ ,  $M$ ,  $Sr$ , and  $Du$ ) quantities on local as well as average Sherwood numbers for  $Al_2O_3$  as well as  $TiO_2$  nanofluids. The local Sherwood number decreases as the values of  $\lambda$ ,  $\epsilon$ , and  $M$  increase. It is observed to have a reverse trend for the remaining parametric values. Since the solute diffuses from one part of elevated species to another region of lower species with a magnitude proportionate to the species gradient, the parameters show a reversal of the trend, which results in a fall in average Sherwood numbers as parameters increase. The numerical predictions for really high porosities (over 0.95) are steadily declining. However, when porosity diminishes, the accuracy of computationally determined Sherwood values declines.

#### 5. Result outcomes

The findings are listed below:

- The velocity and concentration profiles are higher in silver–water nanofluids, whereas the temperature is elevated in copper.
- It is observed that velocity and temperature profiles increase as  $\epsilon$  and  $Rd$  increase, whereas a reverse trend is observed for concentration profiles. Accordingly, it can be observed that if  $M$ , as well as  $\Delta$ ,  $Sr$ , and  $Du$  are raised here, the reverse is true.
- During an enhancement in ( $K$ ), the velocity and temperature stay relatively constant until a gradual decline occurs as the value decreases. A rise in ( $\lambda$ ) reduces concentration.
- Here,  $Al_2O_3$  and  $TiO_2$  experience a decrease in Nusselt number with increasing parameters. The skin friction rises when the parameters for  $Al_2O_3$  and  $TiO_2$  rise, omitting the chemical process, but all other variables except  $Rd$  and  $Du$  enhance the average skin friction.
- As the specified parameters rise, a decline in the local and average rate of mass transfer is noticed.

#### Acknowledgments

The authors are grateful to the editor and reviewers for their valuable suggestions for the improvement of this paper.

#### Disclosure statement

No potential conflict of interest was reported by the author(s).

#### Authors' contributions

ERK, PS, KS, SB, and AJC are responsible for the conception and design of the study. ERK was responsible for carrying out the literature search and drafting the article. PS, KS, and SB all made contributions to the data analysis and interpretation. PS and AJC was the person in charge of supervising the study. All of the writers evaluated and approved the final content.

#### ORCID

Elumalai Ragulkumar  <http://orcid.org/0000-0002-1508-8979>

Paulsamy Sambath  <http://orcid.org/0000-0003-1478-4769>

Ali J. Chamkha  <http://orcid.org/0000-0002-8335-3121>

## References

- [1] S. U. S. Choi and J. A. Eastman, "Enhancing thermal conductivity of fluids with nanoparticles," presented at the CONF-951135-29, No. ANL/MSD/CP-84938, ASME International Mechanical Engineering Congress & Exposition, San Francisco, CA, Nov. 12–17, 1995.
- [2] Y. Xuan and Q. Li, "Heat transfer enhancement of nanofluids," *Int. J. Heat Fluid Flow*, vol. 21, no. 1, pp. 58–64, 2000. DOI: [10.1016/S0142-727X\(99\)00067-3](https://doi.org/10.1016/S0142-727X(99)00067-3).
- [3] S. U. S. Choi, Z. G. Zhang, W. Yu, F. E. Lockwood, and E. A. Grulke, "Anomalous thermal conductivity enhancement in nanotube suspensions," *Appl. Phys. Lett.*, vol. 79, no. 14, pp. 2252–2254, 2001. DOI: [10.1063/1.1408272](https://doi.org/10.1063/1.1408272).
- [4] O. Otegbeye, S. S. Motsa, and M. S. Ansari, "An application of paired quasilinearization on double-diffusive convection flow over a cone embedded in a porous medium in the presence of nanoparticles," *Heat Trans. Asian Res.*, vol. 48, no. 4, pp. 1413–1439, 2019. DOI: [10.1002/htj.21439](https://doi.org/10.1002/htj.21439).
- [5] C. Y. Cheng, "Soret and Dufour effects on natural convection heat and mass transfer from a vertical cone in a porous medium," *Int. Commun. Heat Mass Transf.*, vol. 36, no. 10, pp. 1020–1024, 2009. DOI: [10.1016/j.icheatmasstransfer.2009.07.003](https://doi.org/10.1016/j.icheatmasstransfer.2009.07.003).
- [6] C. Y. Cheng, "Soret and Dufour effects on natural convection boundary layer flow over a vertical cone in a porous medium with constant wall heat and mass fluxes," *Int. Commun. Heat Mass Transf.*, vol. 38, no. 1, pp. 44–48, 2011. DOI: [10.1016/j.icheatmasstransfer.2010.09.011](https://doi.org/10.1016/j.icheatmasstransfer.2010.09.011).
- [7] H. T. Basha, R. Sivaraj, I. L. Animasaun, and O. D. Makinde, "Influence of non-uniform heat source/sink on unsteady chemically reacting nanofluid flow over a cone and plate," *DDF*, vol. 389, pp. 50–59, 2018. DOI: [10.4028/www.scientific.net/DDF.389.50](https://doi.org/10.4028/www.scientific.net/DDF.389.50).
- [8] H. T. Basha, O. D. Makinde, A. Arora, A. Singh, and R. Sivaraj, "Unsteady flow of chemically reacting nanofluid over a cone and plate with heat source/sink," *DDF*, vol. 387, pp. 615–624, 2018. DOI: [10.4028/www.scientific.net/DDF.387.615](https://doi.org/10.4028/www.scientific.net/DDF.387.615).
- [9] V. Buddakkagari and M. Kumar, "Transient boundary layer laminar free convective flow of a nanofluid over a vertical cone/plate," *Int. J. Appl. Comput. Math.*, vol. 1, no. 3, pp. 427–448, 2015. DOI: [10.1007/s40819-015-0027-9](https://doi.org/10.1007/s40819-015-0027-9).
- [10] P. S. Reddy and A. J. Chamkha, "Influence of size, shape, type of nanoparticles, type and temperature of the base fluid on natural convection MHD of nanofluids," *Alex. Eng. J.*, vol. 55, no. 1, pp. 331–341, 2016. DOI: [10.1016/j.aej.2016.01.027](https://doi.org/10.1016/j.aej.2016.01.027).
- [11] P. S. Reddy and A. Chamkha, "Heat and mass transfer analysis in natural convection flow of nanofluid over a vertical cone with chemical reaction," *HFF*, vol. 27, no. 1, pp. 2–22, 2017. DOI: [10.1108/HFF-10-2015-0412](https://doi.org/10.1108/HFF-10-2015-0412).
- [12] P. Sambath, P. Bapuji, T. Hussain, and S. A. Shehzad, "Radiated chemical reaction impacts on natural convective MHD mass transfer flow induced by a vertical cone," *Results Phys.*, vol. 8, pp. 304–315, 2018. DOI: [10.1016/j.rinp.2017.12.005](https://doi.org/10.1016/j.rinp.2017.12.005).
- [13] P. Sambath, P. Bapuji, and R. M. Kannan, "Radiative effects on a free convective mhd flow past a vertically inclined plate with heat source and sink," *J. Phys. conf. Ser.*, vol. 1000, no. 1, pp. 012011, 2018. DOI: [10.1088/1742-6596/1000/1/012011](https://doi.org/10.1088/1742-6596/1000/1/012011).
- [14] P. Sambath, D. S. Sankar, and K. K. Viswanathan, "A numerical study of dissipative chemically reactive radiative MHD flow past a vertical cone with nonuniform mass flux," *Int. J. Appl. Mech. Eng.*, vol. 25, no. 1, pp. 159–176, 2020. DOI: [10.2478/ijame-2020-0011](https://doi.org/10.2478/ijame-2020-0011).
- [15] F. G. Awad, P. Sibanda, S. S. Motsa, and O. D. Makinde, "Convection from an inverted cone in a porous medium with cross-diffusion effects," *Comput. Math. Appl.*, vol. 61, no. 5, pp. 1431–1441, 2011. DOI: [10.1016/j.camwa.2011.01.015](https://doi.org/10.1016/j.camwa.2011.01.015).
- [16] P. Sreedevi, P. S. Reddy, K. V. S. N. Rao, and A. J. Chamkha, "Heat and mass transfer flow over a vertical cone through nanofluid saturated porous medium under convective boundary condition suction/injection," *J. Nanofluids*, vol. 6, no. 3, pp. 478–486, 2017. DOI: [10.1166/jon.2017.1349](https://doi.org/10.1166/jon.2017.1349).
- [17] A. Rashad and A. Chamkha, "Heat and mass transfer by natural convection flow about a truncated cone in porous media with Soret and Dufour effects," *Int. J. Numer. Methods Heat Fluid Flow*, vol. 24, no. 3, pp. 595–612, 2014. DOI: [10.1108/HFF-05-2012-0105](https://doi.org/10.1108/HFF-05-2012-0105).
- [18] P. S. Reddy and A. J. Chamkha, "Soret and Dufour effects on MHD convective flow of Al<sub>2</sub>O<sub>3</sub>–water and TiO<sub>2</sub>–water nanofluids past a stretching sheet in porous media with heat generation/absorption," *Adv. Powder Technol.*, vol. 27, no. 4, pp. 1207–1218, 2016. DOI: [10.1016/j.apt.2016.04.005](https://doi.org/10.1016/j.apt.2016.04.005).
- [19] S. G. Mohiddin, V. K. Varma, and N. Iyengar, "Unsteady viscoelastic free convection boundary layer flow past a vertical cone with uniform heat and mass flux," *J. Comput. Math. Sci.*, vol. 1, no. 2, pp. 103–273, 2010.
- [20] S. G. Mohiddin and S. V. K. Varma, "Numerical study of free convection flow past a vertical cone with variable heat and mass flux," *Int. J. Comput. Appl.*, vol. 56, no. 6, pp. 24–31, 2012.

- [21] E. Ragulkumar, P. Sambath, and A. J. Chamkha, "Free convection nanofluid flow past a vertical isothermal cone surface in the presence of viscous dissipation and MHD with heat flux," *Eur. Phys. J. Plus*, vol. 137, no. 8, pp. 894, 2022. DOI: [10.1140/epjp/s13360-022-03115-6](https://doi.org/10.1140/epjp/s13360-022-03115-6).
- [22] E. Ragulkumar, G. Palani, P. Sambath, and A. J. Chamkha, "Dissipative MHD free convective nanofluid flow past a vertical cone under radiative chemical reaction with mass flux," *Sci. Rep.*, vol. 13, no. 1, pp. 2878, 2023. DOI: [10.1038/s41598-023-28702-0](https://doi.org/10.1038/s41598-023-28702-0).
- [23] P. S. Reddy, A. J. Chamkha, and A. Al-Mudhaf, "MHD heat and mass transfer flow of a nanofluid over an inclined vertical porous plate with radiation and heat generation/absorption," *Adv. Powder Technol.*, vol. 28, no. 3, pp. 1008–1017, 2017. DOI: [10.1016/j.apt.2017.01.005](https://doi.org/10.1016/j.apt.2017.01.005).
- [24] A. J. Chamkha, "Coupled heat and mass transfer by natural convection about a truncated cone in the presence of magnetic field and radiation effects," *Numer. Heat Transf. A: Appl.*, vol. 39, no. 5, pp. 511–530, 2001. DOI: [10.1080/10407780120202](https://doi.org/10.1080/10407780120202).
- [25] A. J. Chamkha, "Non-Darcy fully developed mixed convection in a porous medium channel with heat generation/absorption and hydromagnetic effects," *Numer. Heat Transf. A: Appl.*, vol. 32, no. 6, pp. 653–675, 1997. DOI: [10.1080/10407789708913911](https://doi.org/10.1080/10407789708913911).
- [26] A. J. Chamkha and M. M. A. Quadri Ali, "Heat and mass transfer from a permeable cylinder in a porous medium with magnetic field and heat generation/absorption effects," *Numer. Heat Transf. A: Appl.*, vol. 40, no. 4, pp. 387–401, 2001. DOI: [10.1080/104077801753238167](https://doi.org/10.1080/104077801753238167).
- [27] B. Prabhavathi, P. S. Reddy, R. B. Vijaya, and A. Chamkha, "MHD boundary layer heat and mass transfer flow over a vertical cone embedded in porous media filled with  $Al_2O_3$ -water and Cu-water nanofluid," *J. Nanofluids*, vol. 6, no. 5, pp. 883–891, 2017. DOI: [10.1166/jon.2017.1380](https://doi.org/10.1166/jon.2017.1380).